AIAA AVIATION Forum
8-12 June 2026, San Diego, CA
AIAA AVIATION 2026 Forum

10.2514/6.2026-4739

Numerical Investigation of the Hypersonic Boundary Layer Transition over a Blunt Cone using High-Order Discontinuous Galerkin Methods and Stability Theories

Antoine Ghyoot*[1,2,4], Vincenzo Romano†[1,2], Alberto Testa‡[1,2], Gianmario Perrucci§[1,2]

David Henneaux¶[5], *Pierre Schrooyen*‖[2]

*Koen Hillewaert***[3,4,5], *Olivier Chazot*††[2], *Thierry Magin*‡‡[1,2]

[1] *Department of Aero-Thermo Mechanics, Université Libre de Bruxelles, Brussels, 1050, Belgium*
[2] *Aeronautics & Aerospace Department, von Karman Institute for Fluid Dynamics, Rhode-Saint-Genèse, 1640, Belgium*
[3] *Turbomachinery & Propulsion Department, von Karman Institute for Fluid Dynamics, Rhode-Saint-Genèse, 1640, Belgium*
[4] *Aerospatial & Mechanics Department, Université de Liège, Liège, 4000, Belgium*
[5] *Cenaero, Charleroi, 6041, Belgium*

This study investigates the hypersonic boundary layer transition over a blunt cone using high-order Discontinuous Galerkin methods and stability theories. The receptivity of the boundary layer to freestream acoustic disturbances is modeled through a two-dimensional axisymmetric Direct Numerical Simulation performed with the ArgoDG solver. A combination of fast and slow acoustic waves at a single frequency is considered. The imposed disturbances induce the growth of second-mode instability, which is the most dominant instability leading to transition to turbulence for the geometry and the flow conditions considered in this work. The onset of nonlinear interactions, which manifest as the characteristics rope-like structures and the generation of higher harmonics, as well as characteristic wall pressure fluctuations are also observed. The perturbations remain consistent with the predictions of Linear Stability Theory as long as nonlinear effects are weak. Once nonlinearities become significant, the two-dimensional axisymmetric Direct Numerical Simulation results align with those obtained from the Nonlinear Parabolized Stability Equations. Comparisons with the numerical results show consistent behavior in both the receptivity region and the phase of harmonics generation in the nonlinear region.

I. Nomenclature

Greek symbols

α = Streamwise wavenumber
β = Spanwise wavenumber
δ = Dirac delta
ε = Amplitude small parameter

---

*Ph.D. Candidate, Department of Aero-Thermo Mechanics (Université Libre de Bruxelles), Aeronautics & Aerospace Department (von Karman Institute for Fluid Dynamics), and Aerospatial & Mechanics Department (Université de Liège), antoine.ghyoot@ulb.be

†Ph.D. Candidate, Department of Aero-Thermo Mechanics (Université Libre de Bruxelles), and Aeronautics & Aerospace Department (von Karman Institute for Fluid Dynamics), vincenzo.romano@ulb.be

‡Ph.D. Candidate, Department of Aero-Thermo Mechanics (Université Libre de Bruxelles), and Aeronautics & Aerospace Department (von Karman Institute for Fluid Dynamics), alberto.testa@ulb.be

§Ph.D. Candidate, Department of Aero-Thermo Mechanics (Université Libre de Bruxelles), and Aeronautics & Aerospace Department (von Karman Institute for Fluid Dynamics), gianmario.perrucci@ulb.be

¶Senior Research Engineer, Cenaero, david.henneaux@cenaero.be

‖Assistant Professor, Aeronautics & Aerospace Department, von Karman Institute for Fluid Dynamics, pierre.schrooyen@vki.ac.be

**Associate Professor, Aerospatial & Mechanics Department (Université de Liège), koen.hillewaert@ulg.be

††Full Professor and Head of Aeronautics & Aerospace Department, von Karman Institute for Fluid Dynamics, olivier.chazot@vki.ac.be

‡‡Full Professor, Department of Aero-Thermo Mechanics (Université Libre de Bruxelles), thierry.magin@ulb.be

θ = Half-cone angle
μ = Dynamic viscosity
μ_{bulk} = Bulk viscosity
ρ = Density
τ = Shear stress tensor
ω = Angular frequency
ξ, η, ζ = Curvilinear coordinate system

Roman symbols

dt = Timestep
f = Frequency
$\mathbf{f}$ = Nonlinear forcing
k_x = Axial wave number component
k_y = Radial wave number component
m = Spanwise/azimuthal mode
n = Temporal mode
M = Mach number
p = Pressure
Pr = Prandtl number
Re = Reynolds number
t = Time
T = Temperature
u = Axial velocity component
v = Radial velocity component
x, y, z = Cartesian coordinates system

Superscripts

$'$ = Fluctuating quantity
$*$ = Normalized quantity
$-$ = Mean quantity

Subscripts

∞ = Far-field quantity
$\langle n, 0\rangle$ = Temporal mode n, or harmonic n
b = Base-flow quantity

II. Introduction

The Boundary Layer (BL) transition from laminar to turbulent flow in hypersonic regime has attracted significant attention over the past years, due to its high impact on the aero-thermal load of high-speed vehicles. One of the key factors of BL transition is the nonlinear response of the fluid system to forcing environmental disturbances [1]. A mismatch is often retrieved between ground testing and in-flight predictions. The latter is mainly due to pressure waves radiated by the turbulent BL of nozzle walls in conventional wind tunnels [2], which affect the BL developing over the tested sample. At high Mach numbers, BL transition is mainly driven by the second mode instability[*], which is most amplified when two-dimensional [3]. Therefore, a good understanding of the second mode growth is crucial for the design of any high-speed body. To this end, the current paper aims to study the effects of wind tunnel-like freestream noise on the transition process over the canonical hypersonic blunt cone configuration, under the H3 conditions, the Mach 6 blowdown wind tunnel at the von Karman Institute (VKI). The high-fidelity discontinuous Galerkin (DG) solver ArgoDG [4] is used to perform a 2D axisymmetric Direct Numerical Simulation (2D DNS) with a wind tunnel-like

---

[*] This is valid in case of low bluntness, no angle of attack and no concave streamlines. Otherwise, other instabilities can be dominant, such as crossflow, Görtler and the nonmodal streaks. Moreover, in case of very hot walls, the first mode might be more amplified than the second one.

injection of acoustic disturbances to model the BL receptivity mechanism. The advantages of DG methods compared to conventional finite volume solvers relies on its spatial discretization which allows low dissipation and dispersion properties, the ability to locally adapt both grid size and the interpolation order, and the high order convergence on unstructured grids. These features are particularly well suited for simulating multi-scale problems, such as flows involving transitional processes. In addition, DG methods are well-suited to high-performance computing due to their high flop-to-communication ratio. Note that hypersonic applications have already been carried out with ArgoDG [5], but few verification test cases were performed. In that scope, the steady solution obtained with ArgoDG is compared with the state-of-the-art finite volume solver US3D. Furthermore, the results obtained with ArgoDG for the unsteady computations (i.e. with noise injection) are compared with the estimations of the flow perturbations based on the Linear Stability Theory (LST) and the Nonlinear Parabolized Stability Equation (NPSE) retrieved from the VESTA toolkit (VKI Extensible Stability and Transition Analysis) [6]. The distinctiveness of the present study lies in its integrated approach combining stability analysis and high-order/fidelity simulations to analyse hypersonic BL transition. Moreover, to the best of our knowledge, the influence of DG stabilization techniques — such as numerical flux choices or shock-capturing strategies — on the accurate prediction of acoustic mode amplification has received little to no dedicated attention and will therefore also be investigated.

The paper is organized as follows: the numerical setup and the flow conditions for the base-flow simulation performed with ArgoDG along with the model for the injection of freestream acoustic disturbances are presented in Section III. Then, the stabilization methods for the shock treatment and the stability theories used in this work are described in Section IV. Finally, comparisons between the ArgoDG/US3D base-flow solutions, and comments between the 2D DNS simulation and the predictions from LST and NPSE are proposed in Section V.

III. Numerical Setup and Flow Conditions

The first two subsections detail the flow conditions and the cone geometry that were used to obtain the base-flow solution. The base-flow solution will be required for both the BL stability computations and the 2D DNS unsteady simulation with tunnel-like noise injection. These tunnel-like freestream acoustic disturbances will be prescribed as time-dependent inlet boundary conditions, and are described in the last subsection.

A. Configuration and Freestream Conditions

The geometry of interest is a blunt cone, characterized by a nose radius of $R_{\mathrm{N}} = 0.126$ mm, an axial length of $L_{\mathrm{cone}} = 265$ mm, and half-cone angle of $\theta = 7$ degrees. At the wall, the standard no-slip condition is applied along with an isothermal temperature $T_{\mathrm{w}} = 295$ K. The freestream conditions are those of the VKI H3 facility [7], which are summarized in Tab. 1. In particular, the air is assumed to behave as a calorically perfect gas with $\gamma = 1.4$, the dynamic viscosity is computed with Sutherland's law, and the thermal conductivity is retrieved by the Prandtl number, which is kept constant.

$\bar{M}_\infty[-]$	$\bar{p}_\infty[Pa]$	$\bar{T}_\infty[K]$	Pr	$Re_{\infty,\mathrm{unit}}[1/\mathrm{m}]$
6	1358.69	60.975	0.7368	18×10^6

Table 1 VKI H3 freestream conditions.

In the following, (ξ, η, ζ) refers to a body-fitted coordinate system, where ξ is the streamwise coordinate along the cone surface, η is the coordinate normal to the surface of the cone, and ζ is the spanwise direction, which in this case (axisymmetric configuration) is the azimuthal direction. Instead, (x, y, z) is the cartesian reference frame, where x is the coordinate aligned with the cone axis, y is the radial coordinate normal to the cone axis, and z is the coordinate out of the cone plane.

B. Laminar steady-state base flow

The numerical setup for the two-dimensional axisymmetric simulation is represented in Fig. 1. A symmetry condition is forced at the stagnation line while the flow at the outlet is treated with a zero-gradient boundary condition. In order to satisfy the outlet condition, the domain has been extended, where a slip condition on the wall has been applied to ensure a supersonic regime over the entire height of the outlet.

Unlike the continuous finite element methods, no continuity is imposed at the boundaries of the mesh elements. This allows the possibility to adapt the interpolation order depending on the regions of interest. As it will be presented in Section III.C, the BL receptivity mechanism to incoming freestream noise perturbations is studied. To benefit from resolution capabilities of the high-order scheme, a fourth interpolation order is applied in the BL region (green dashed

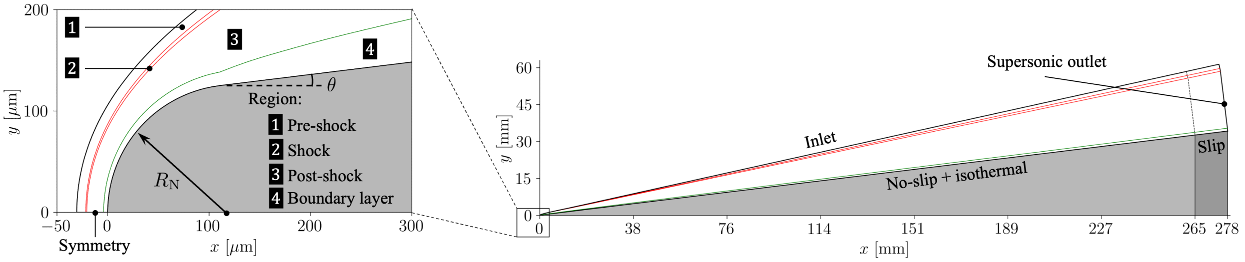

Fig. 1 Numerical setup for the high-order two-dimensional axisymmetric base-flow obtained with ArgoDG.

line in Fig. 1). The post-shock region until the BL and the pre-shock region are captured with a second interpolation order. The shock region is captured at a zeroth interpolation order for the reasons explained in Section IV.A.1. Given the computational cost of the simulation, computations were performed on several MPI ranks. Because of the uneven repartition of the degrees of freedom in the domain due to order adaptation, a proper balancing of the mesh partitioning is required to ensure scalability of the solver. Hence, a static load balancing, based on the interpolation order of the elements, is performed at the initialization of the problem, as shown in Fig. 2. The spatial inviscid flux are computed using the SLAU scheme [8]. As mentioned in [5], attention must be paid to the discretization of the diffusive part to ensure consistency when using a limiting approach degrading the interpolation order to zero. Therefore, the Bassi-Rebay 2 method is used to compute the diffusive flux. Finally, the implicit second order backward differentiation formula is used for time integration, for both the steady and unsteady simulations.

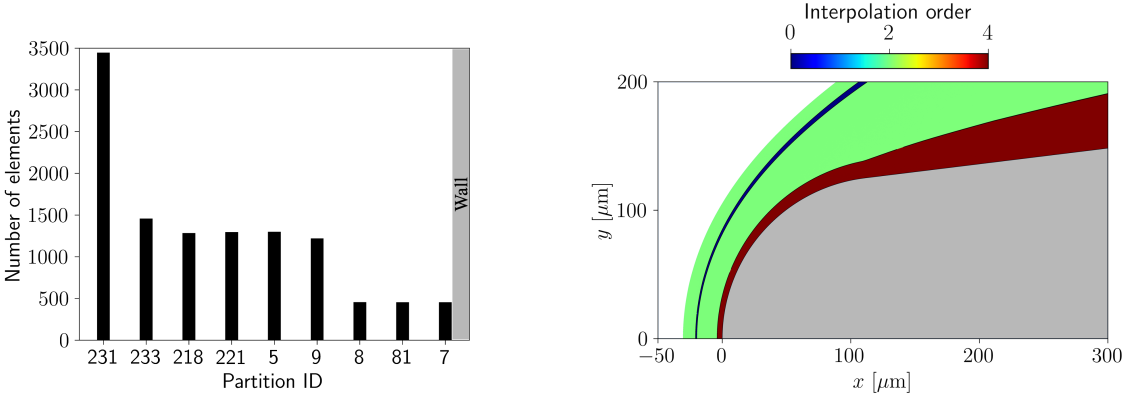

Fig. 2 Static load balancing of the partitions for the high-order computations. The number of elements per partition on the stagnation line is represented on the left, and the order adaption on the right.

C. Freestream Acoustic Disturbances

The BL receptivity to wind tunnel-like noise has been investigated. Two kinds of freestream disturbances, fast acoustic waves and slow acoustic waves, with a single frequency $f = 450$ kHz were considered. The choice for this value for the frequency is motivated by preliminary LST results [9], as explained in Sec. V.A. These perturbations were modeled as time dependent inlet boundary conditions where a timestep $dt = 10^{-8}$ second has been chosen such that one oscillation of the incoming perturbations are discretized by approximately 220 timesteps. The grid spatial discretization is such that one wavelength is represented by 15 interpolation points. This grid resolution in the BL is based on the grid convergence conducted by Romano et al. [9]. In case of ± signs in relevant component of the following expressions, the top sign represents the fast acoustic wave and the bottom sign represents the slow acoustic waves. The instantaneous quantities at the inlet boundary due to the disturbances at time t can be defined as

$$\begin{bmatrix} p \\ T \\ u \\ v \end{bmatrix}_\infty = \begin{bmatrix} \bar{p} \\ \bar{T} \\ \bar{u} \\ \bar{v} \end{bmatrix}_\infty + \sum \begin{bmatrix} |p'| \\ |T'| \\ |u'| \\ |v'| \end{bmatrix}_\infty e^{i\left[k_x(x-a)+k_y(y-b)-\omega t\right]}, \tag{1}$$

where the subscript $(_\infty)$ denotes far-field quantities, while the notations $(\bar{\cdot})$ and $(\cdot')$ represent mean flow quantities and the perturbations, respectively. The perturbations are considered with an angle of incidence of zero such that the following expressions holds for k_x and k_y, the spatial wave number components in cartesian coordinates

$$k_y = 0, \quad k_x = k_\infty, \quad \text{where} \quad k_\infty = \frac{\bar{M}_\infty \omega}{\bar{u}_\infty \left(\bar{M}_\infty \pm 1\right)}, \tag{2}$$

with k_∞ the absolute wave number and $\omega = 2\pi f$ the angular frequency of the freestream disturbances. The source of the perturbations is located far from the body at $(a, b) = (-L_{\text{cone}}, 0)$ and their amplitudes, denoted as $(|\cdot'|)$, are defined as [10]

$$\begin{aligned} |p'| &= \varepsilon \bar{\rho}_\infty \bar{u}_\infty^2, & |u'| &= \pm \varepsilon \bar{M}_\infty \bar{u}_\infty, \\ |T'| &= \varepsilon (\gamma - 1) \bar{M}_\infty^2 \bar{T}_\infty, & |v'| &= 0. \end{aligned} \tag{3}$$

In Eqs. 3, the amplitudes of the perturbations are characterized by the small parameter ε. Initially, three values for the amplitude were investigated: $\varepsilon = 1 \cdot 10^{-4}$, $\varepsilon = 5 \cdot 10^{-5}$ and $\varepsilon = 1 \cdot 10^{-5}$. However, only the lowest amplitude has been considered as it was sufficient to trigger perturbations amplification while ensuring the longest part of the cone under a linear receptivity process.

IV. Numerical Models and Stability Equations

Capturing under-resolved features of the flow, such as shocks, remains an open challenge for high-order DG schemes [11]. Given its blunted shape, a bow shock forms in front of the body, therefore requiring a robust strategy to capture it to avoid Gibb's oscillations and thus, the possible breakdown of the simulation. The first subsection will present the two methods used in the scope of this work to capture the shock in order to stabilize the solution. The second subsection describes the two stability methods employed to estimate instability behavior in the BL transition process.

A. Shock Capturing Methods

Various methods are available to stabilize the solutions when using DG methods, and they can generally be classified based on whether they alter the numerical scheme (e.g. entropy stable methods [12], limiting methods [5]) or the underlying physical equations (e.g. Laplacian- and physics-based artificial viscosity [13]). In this work, both types of methods are used. The first method presented is a limiting approach consisting in locally reducing the polynomial order to capture the shock. The second method relies on adding artificial viscosity in the shock vicinity where a physics-based sensor is of use.

1. Limiting

The limiting approach consists in reducing the order of convergence in the shock region to first order (constant value in the cell) in view of capturing the shock while preserving the monotocity of the scheme [5]. To alleviate the decrease of accuracy in the shock region, mesh refinement tailored to the shock position (red dashed line in Fig. 1) is performed iteratively. To obtain the position of the shock, a cubic spline interpolation is performed where the control points are given by the local maxima of the temperature gradient along the wall normal.

2. Physic-based Artificial Viscosity

Artificial viscosity (AV) introduces tailored numerical diffusion that smooths discontinuities such as shock waves. This enables high-order solutions to capture the phenomena without being affected by Gibbs' instabilities. The concept was first proposed in 1949 by von Neumann et al. [14]. In contrast to other shock capturing approaches that modify the numerical discretization, such as entropy stable schemes [15] and sub-cell limiting [16], AV acts directly on the governing equations. This results in an easier implementation, low computational cost, and strong robustness. However, depending on the specific formulation, AV may degrade the solution in smooth regions, and it can be sensitive to user defined parameters that are often difficult to tune [17].

Among the different AV methods, the Physics-based Artificial Viscosity (PAV) introduced by Fernandez et al. [18] provides a novel mechanism to introduce numerical diffusion. The method modifies the formulation of the shear stress tensor by introducing the numerical viscosity as the bulk viscosity μ_{bulk}:

$$\tau_{ij} = \mu \left[\left(\frac{\partial v_i}{\partial x_j} + \frac{\partial v_j}{\partial x_i} \right) - \frac{2}{3} \frac{\partial v_k}{\partial x_k} \delta_{ij} \right] + \mu_{bulk} \frac{\partial v_k}{\partial x_k} \delta_{ij}. \tag{4}$$

This approach exhibits several desirable properties, including reduced dissipation of vortical structures. It differs significantly from more classical methods, where numerical diffusion is introduced using a Laplacian source term [13].

Artificial Viscosity is applied only to troubled cells, which are identified using a shock sensor. Several options are available [19, 20]. The ArgoDG solver can employ a dilatation-based sensor [18], which detects shocks by identifying regions where the flow undergoes sudden deceleration, or a modal decay sensor [13], which identifies regions of the domain most sensitive to the polynomial order of the solution. Both formulations depend on user-defined parameters, which are typically determined iteratively. Automatically determining the optimal coefficients is subject of current study.

B. Boundary Layer Stability Analyses

The current section describes the BL stability analyses performed for comparison with the 2D DNS results. In particular, the small perturbation assumption is presented, which is the basis of most of stability theories, the Linear Stability Theory (LST) and the Nonlinear Parabolized Stability Equations (NPSE).

1. Navier-Stokes Equations with the Small Perturbation Assumption

BL stability theories consist in writing the state vector of fluid dynamic Navier-Stokes (NS) equations as the sum of the steady-state laminar solution or base-flow $\bar{\boldsymbol{q}}_b$ and a perturbation $\boldsymbol{q}'$, with the assumption that the perturbation is much smaller than the base-flow (small perturbation assumption):

$$\boldsymbol{q} = \bar{\boldsymbol{q}}_b + \boldsymbol{q}' \qquad \boldsymbol{q}' \ll \bar{\boldsymbol{q}}_b. \tag{5}$$

Substituting Equation 5 into NS equations, and performing a Taylor expansion, the following relation is reached:

$$\frac{\partial\left(\bar{\boldsymbol{q}}_b + \boldsymbol{q}'\right)}{\partial t} = \mathbf{NS}\left(\bar{\boldsymbol{q}}_b + \boldsymbol{q}'\right) \rightarrow \frac{\partial \boldsymbol{q}'}{\partial t} = \boldsymbol{J}\boldsymbol{q}' + H.O.T. \tag{6}$$

where $\boldsymbol{J} = \partial \mathbf{NS}/\partial \boldsymbol{q}|_{\bar{\boldsymbol{q}}_b}$ is the Jacobian operator or the linearized NS operator and $H.O.T.$ denotes the Higher Order Terms. The BL stability analyses are conducted with the VKI in-house stability tool VESTA.

2. Linear Stability Theory (LST)

The LST [21] assumes that the base flow is locally parallel, i.e. $\bar{\boldsymbol{q}}_b = \bar{\boldsymbol{q}}_b(\eta)$, and neglects the $H.O.T.$ Therefore, performing a BL-LST analysis means solving the linear dynamics of the perturbations. At this point, LST assumes wave-like perturbations, which can be shown to correspond to orthogonal modes:

$$\boldsymbol{q}'(\xi, \eta, \zeta, t) = \hat{\boldsymbol{q}}(\eta) e^{i(\alpha\xi + \beta\zeta - \omega t)}, \tag{7}$$

where α and β are the streamwise and spanwise wavenumbers, respectively. Here, $\omega = 2\pi f$ is the angular frequency, where f is the frequency. Inserting Equation 7 in Equation 6, the analysis leads to an eigenvalue problem for the Jacobian operator. To solve the spatial stability problem, the frequency and spanwise wavenumber are specified and real-valued, and the streamwise wavenumber is the complex eigenvalue unknown. Instead, $\hat{\boldsymbol{q}}(\eta)$ is the complex eigenfunction, which gives the mode shape through the BL. The nature of instability depends on the sign of the imaginary part of the streamwise wavenumber ($\Im(\alpha)$). The opposite of $\Im(\alpha)$ is referred to by *the streamwise growth rate*. It could be positive, negative or null, which correspond to a damped, amplified or neutral wave, respectively. The integration of the streamwise growth rate gives the well known $N-$factor, which is a measure of the instability amplitude:

$$N = -\int_{\xi_0}^{\xi} \Im\left(\alpha\left(\chi\right)\right) \, d\chi, \tag{8}$$

where x_0 is the neutral point, so the first point where $\Im(\alpha) = 0$. As described above, LST is a linear formulation and thus does not provide information about where transition occurs. To determine this, the e^N-method [22] can be applied. However, the current paper aims to analyze only the instability behavior, without any transition estimation.

3. Nonlinear Parabolized Stability Equations (NPSE)

LST provides a first-order description of infinitesimal disturbance amplification. However, its local and linear assumptions limit its ability to capture non-parallel effects and nonlinear mode interactions. To overcome these limitations, the NPSE [23] extend the same perturbation framework by reintroducing the $H.O.T.$ in a controlled, parabolized form. Starting from Eq. 6, the NPSE assume that the perturbations evolve slowly along the streamwise direction while remaining periodic in time and in the spanwise coordinate. The disturbance field is expressed as a truncated Fourier series in the azimuthal direction ζ and in time t:

$$\boldsymbol{q}'\,(\xi,\eta,\zeta,t) = \sum_{n=-N}^{N}\sum_{m=-M}^{M} \check{\boldsymbol{q}}(\xi,\eta)_{\langle n,m\rangle}\, e^{i(m\beta_0\zeta - n\omega_0 t)}, \tag{9}$$

where n and m denote the temporal and spanwise (or azimuthal) modes, respectively. A wave-like ansatz is then introduced for each harmonic amplitude to describe its slow streamwise evolution:

$$\check{\boldsymbol{q}}(\xi,\eta)_{\langle n,m\rangle} = \hat{\boldsymbol{q}}(\xi,\eta)_{\langle n,m\rangle}\exp\left(i\int_{\xi_0}^{\xi}\alpha_{n,m}(\chi)\,d\chi\right), \tag{10}$$

where $\hat{\boldsymbol{q}}(\xi,\eta)_{\langle n,m\rangle}$ represents the slowly varying shape function and $\alpha_{n,m}$ the complex streamwise wavenumber. Substituting this expression into the NS equations and neglecting the second-order streamwise derivatives of the perturbations yields a set of parabolized equations for each harmonic in compact matrix form:

$$\boldsymbol{L}\hat{\boldsymbol{q}} + \boldsymbol{M}\frac{\partial\hat{\boldsymbol{q}}}{\partial\xi} + \frac{\partial\alpha}{\partial\xi}\boldsymbol{N}\hat{\boldsymbol{q}} = \boldsymbol{f}_{\langle n,m\rangle}, \tag{11}$$

where the $\boldsymbol{L}$, $\boldsymbol{M}$ and $\boldsymbol{N}$ matrices are in general functions of the base-flow quantities and the disturbance parameters α,β and ω, while $\boldsymbol{f}_{\langle n,m\rangle}$ is the nonlinear forcing term arising from mode coupling–thus accounting for the previously neglected higher-order interactions. This formulation allows the evolution of finite-amplitude disturbances over extended streamwise distances while maintaining computational efficiency. The transition onset can be identified directly as the location where the skin-friction coefficient deviates from its laminar value, indicating the amplification of nonlinear effects. Although NPSE captures both non-parallel and nonlinear mechanisms, its parabolic nature limits applicability to flows dominated by streamwise evolution; fully turbulent breakdown and strong shock-BL interactions still require advanced methods. Nevertheless, the NPSE framework provides a robust bridge between linear theories and high-fidelity simulations, capturing essential features of the nonlinear transition process.

V. Results

A. Laminar Solution

For validation purposes, the high-order steady state solutions obtained with ArgoDG with the limiting approach and the physic-based artificial viscosity have been compared with the steady state solution computed with the state-of-the-art hypersonic solver US3D [24], developed by the University of Minnesota. US3D is a three-dimensional cell-centered Finite Volume software that has been run using a 2^{nd} order MUSCL (Monotonic Upstream-Centered Scheme for Conservation Laws) scheme. To simulate the axisymmetric conditions, the two-dimensional fluid domain has been discretized, and then the mesh has been rotated of a half-degree around the cone axis. A symmetry condition was applied to the extruded face to simulate body axisymmetry. To reach a good solution an iterative process has been followed. A tentative mesh has been created, and then the US3D code has been run for a number of iterations, allowing the bow shock to stabilize in front of the cone. At this point, the shock wave has been extracted, the mesh aligned with the shock, and then US3D has been converged. The whole procedure has been controlled by the VKI-internal library HEROES [25].

To ensure a consistent comparison, both steady simulations are computed with 3 million degrees of freedom. The solutions in the nose region and along the cone are compared in Fig. 3 and Fig. 4, respectively. As one can observe, the solutions obtained with both stabilization methods show excellent agreements with the one of US3D. Furthermore, given the similarity between the solutions obtained with both stabilization techniques and with the motivation of reducing the computational cost, the base-flow obtained with the limiting approach has been used for the unsteady simulation with the injection of acoustic disturbances. However, the limiting approach showed a drastic dissipation of the acoustic disturbances across the shock layer. This drawback is discussed in the following section. Once the base-flow with the limiting approach has been obtained, a preliminary LST study for the second mode instability has been performed. The results of this study are shown in Fig. 5, where frequencies ranging from 400 kHz to 1800 kHz were considered. As one can observe, the frequency $f = 450$ kHz leads to the highest N-factor. Therefore, this frequency has been used for the noise injection model presented in Sec. III.C. These results are in line with the work conducted by Romano et al. [9] on the same geometry and for the same flow conditions.

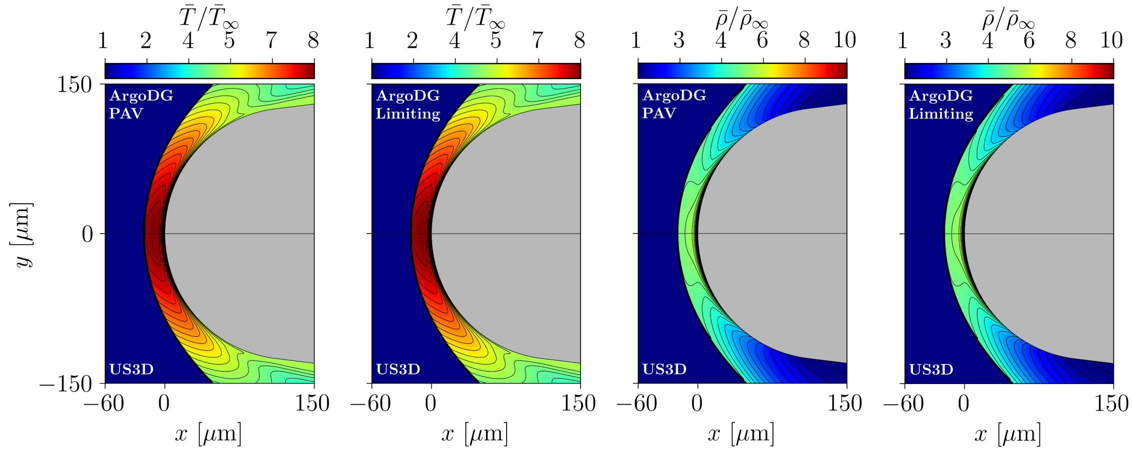

Fig. 3 Comparison of temperature and density contours of the laminar base-flow solutions in the nose region computed by US3D and ArgoDG. In the case of ArgoDG, the solutions obtained with the limiting approach and the physic-based artificial viscosity to stabilize the shock are also compared.

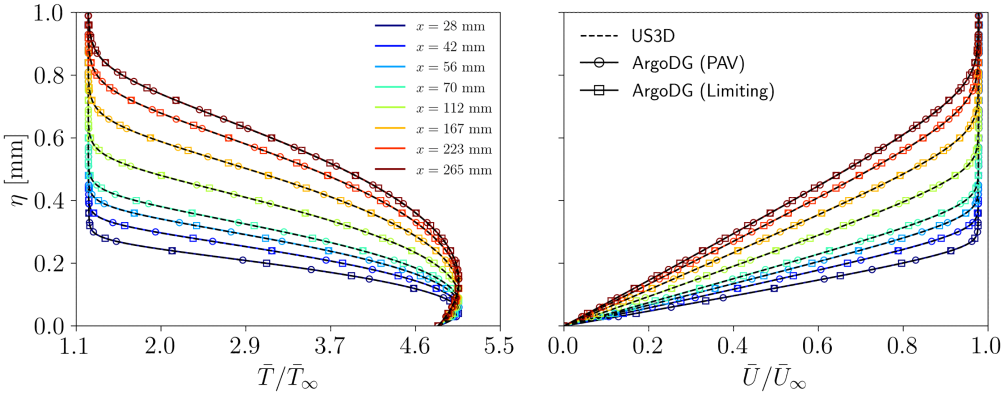

Fig. 4 Comparison of boundary layer profiles of the laminar base-flow solutions computed by US3D and ArgoDG. In the case of ArgoDG, the solutions obtained with the limiting approach and the physic-based artificial viscosity to stabilize the shock are also compared.

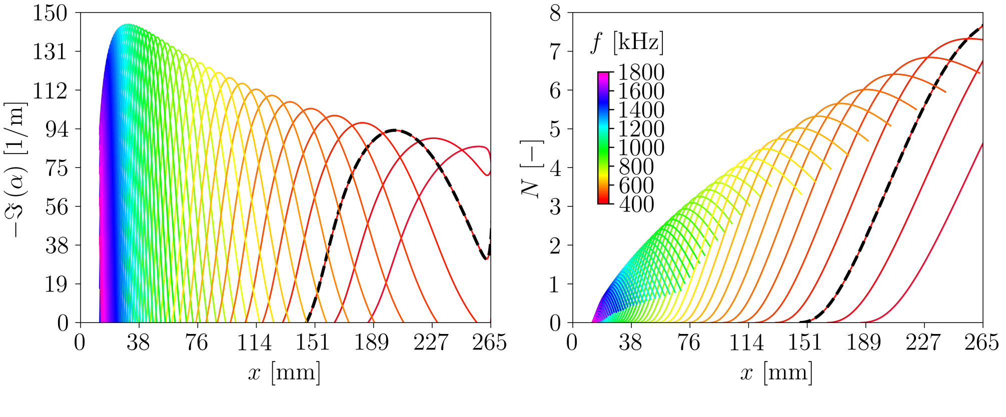

Fig. 5 Growth rates (left) and N-factor (right) curves predicted by the LST for frequencies ranging from 400 kHz to 1800 kHz with increments of 25 kHz. The frequency f = 450 kHz considered for the injection model of the 2D DNS is highlighted with a black dashed line.

B. Boundary Layer Receptivity to Slow and Fast Acoustic Waves

The impact of fast and slow acoustic waves on the development of the second mode has been investigated using high-order unsteady computations. The simulation with noise injection has been restarted from the steady solution obtained with ArgoDG with the limiting approach where the time dependent boundary conditions described in Section III.C have been switched on during a period of time of 1 ms. This time period ensures at least three convective times of the incoming perturbations along the domain, where the convective velocity is taken as 90% of the BL edge velocity. The resulting pressure perturbations field at the final time step of the simulation can be observed in Fig. 6, where the impact of the limiting approach on the dissipation of perturbations passing the shock can be clearly noticed. Note that the level of dissipation tends to drastically decrease in the nose region due to a finer mesh. Moreover, the jump of interpolation order between the shock layer and the post-shock region (i.e. the jump between a constant to a non-constant solution across two grid elements) creates weak but non-physical perturbations. These drawbacks of the limiting approach for such simulations motivate the use of stabilization techniques that are less dissipative and that allow high-order schemes in under-resolved regions (i.e. shocks). The presence of the second mode instability is confirmed by the well-known observed rope-like structures inside the BL, as shown in Fig. 7, and in Fig. 8. The former depicts the temperature fluctuations T', whereas the latter shows the numerical schlieren in terms of the density gradient. Here, one can also note the trapped acoustic waves that are reflected by both the cone wall and the relative sonic line [26]: this highlights the acoustic nature of the second mode instability.

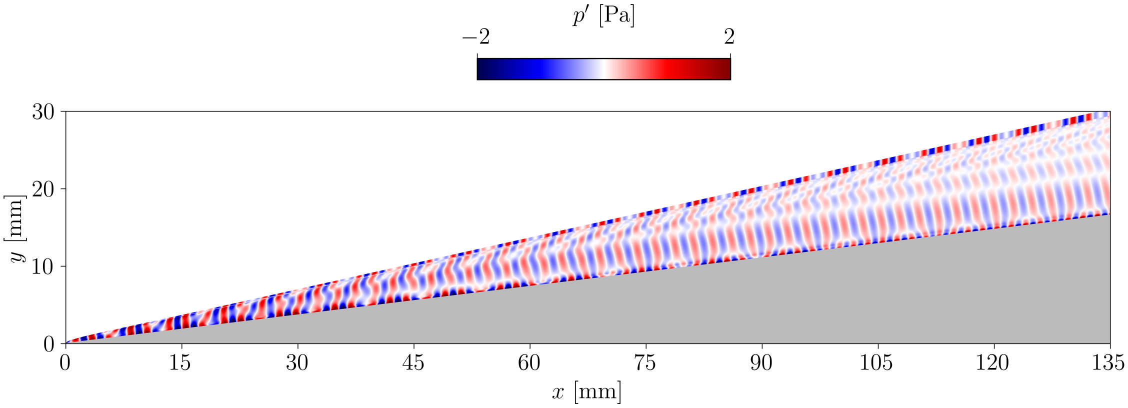

Fig. 6 Instantaneous pressure perturbations generated by freestream fast and slow acoustic waves at t = 1 ms.

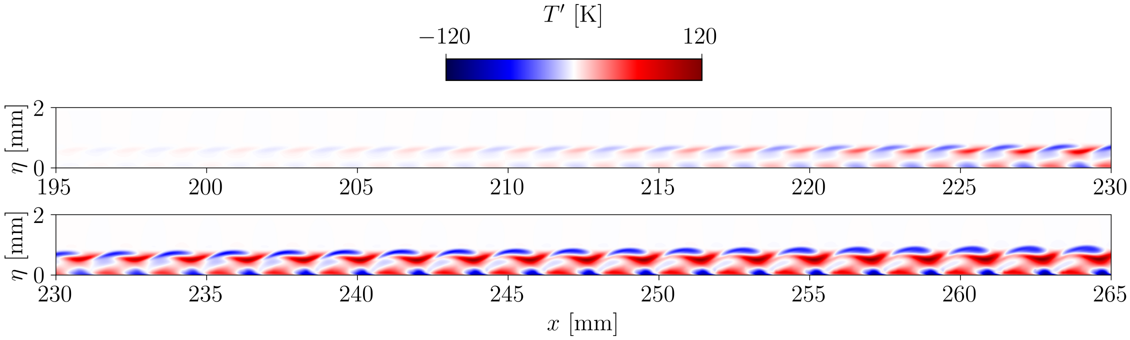

Fig. 7 Contours of temperature perturbations between x = 195 mm and x = 265 mm at t = 1 ms.

In what follows, harmonics will be denoted as $f_{\langle n,m\rangle}$ where n corresponds to the temporal mode (or the level of the harmonic), and $m = 0$ as no azimuthal modes are considered. For example, the frequency of the perturbations that are injected at the inlet is denoted as $f_{\langle 1,0\rangle} = 450$ kHz and referred as the main frequency. For the 2D DNS, a perturbation is given as $(\cdot') = (\bar{\cdot}) - (\cdot)$, and its amplitude is denoted as $|\cdot'|$. The amplitude of the perturbation for a given harmonic $f_{\langle n,0\rangle}$ is extracted using a Fast Fourier Transform and is designated as $|\cdot'|_{\langle n,0\rangle}$. In relevant cases, the superscript $(^*)$ represents the normalization by the maximum amplitude corresponding to the harmonic referred in the subscript. If no harmonic is indicated in the subscript, the normalization is based on the main frequency $f_{\langle 1,0\rangle}$. Fig. 9 shows the normalized amplitude of the wall pressure perturbations. First, one can observe destructive and constructive

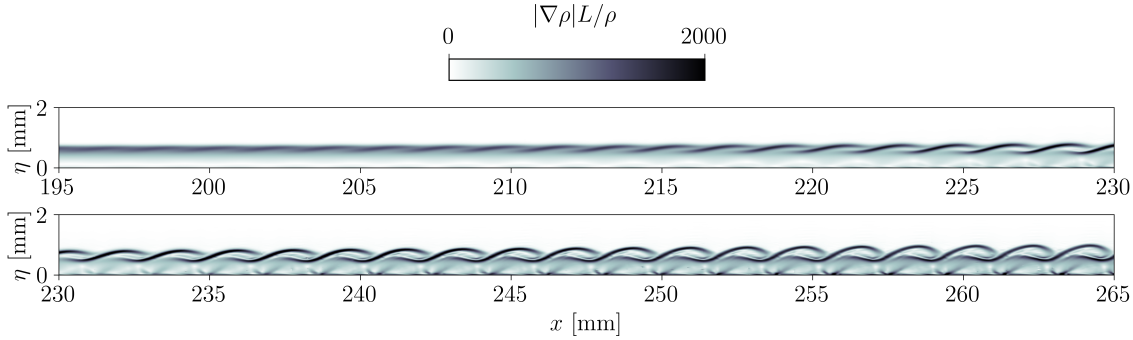

Fig. 8 Contours of the numerical schlieren between x = 195 mm and x = 265 mm at t = 1 ms.

interactions at a relatively constant amplitude between the two types of perturbations from the nose region up to $x \approx 155$ mm. Amplification of the perturbations amplitude related to the main frequency $f_{\langle 1,0\rangle}$ can be observed at $x \approx 155$ mm, marking the beginning of the linear growth. The first higher harmonic $f_{\langle 2,0\rangle} = 900$ kHz is generated at $x \approx 185$ mm, then followed by the excitation of the higher harmonics at $x \approx 215$ mm showing nonlinearities in the flow-field. As mentioned in [27], the generation of higher harmonics is likely due to self-interactions of the second mode disturbances. In fact, first level interactions between the slow and fast acoustic waves would generate the first higher harmonic ($\langle 1,0\rangle + \langle 1,0\rangle = \langle 2,0\rangle$). Then, interactions between the main frequency and the first higher harmonic would lead to second level interactions and the generation of the second higher harmonic $f_{\langle 3,0\rangle} = 1350$ kHz ($\langle 1,0\rangle + \langle 2,0\rangle = \langle 3,0\rangle$). This process of second level interactions can be extended to even higher levels of harmonics, therefore explaining the appearance of the harmonics $f_{\langle 4,0\rangle} = 1800$ kHz, $f_{\langle 5,0\rangle} = 2250$ kHz and $f_{\langle 6,0\rangle} = 2700$ kHz. The emergence of the first and second level interactions marks the beginning of the nonlinear state of the modal growth of the perturbations in the BL.

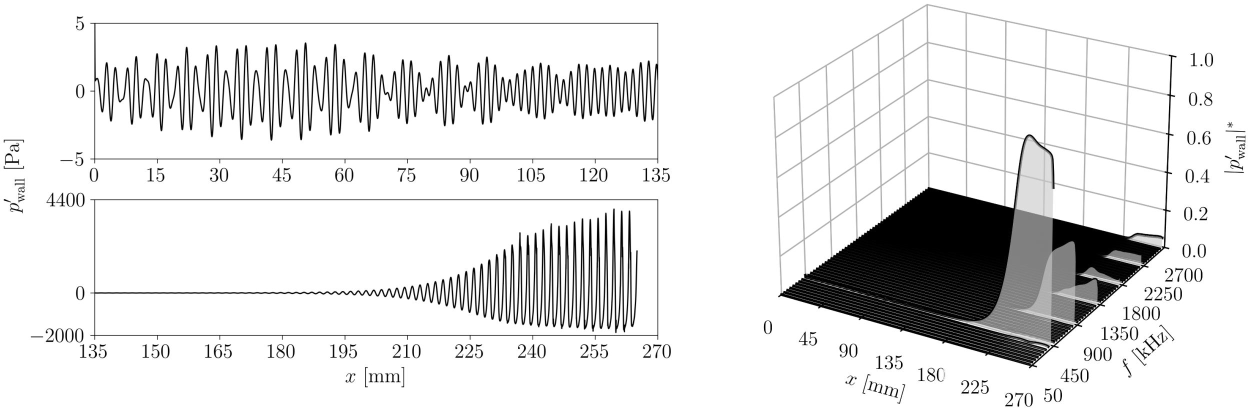

Fig. 9 Instantaneous wall pressure fluctuations at t = 1 ms (left) and spectral distribution of the normalized amplitude of the wall pressure perturbations (right) along the axial direction of the cone.

Fig. 10 compares the normalized amplitudes of the temperature, pressure and velocities profiles along the wall normal direction obtained by LST, NPSE and the 2D DNS. Three stations were chosen for comparison. While the first station ($x = 180$ mm) corresponds to a location where nonlinearities are not yet developed, the two other stations ($x = 220$ mm and $x = 245$ mm) are respectively located just before and after the nonlinear saturation near the end of the cone. As mentioned in Section IV.B.3, the stability analysis performed by the NPSE is based on the injection of a wave-like ansatz at a given location x_i in the BL. The shape functions of the perturbations at the station x_i are obtained from LST as normalized profiles with respect to a desired quantity [28]. In general, these profiles are then dimensionalized by an arbitrary, or tuned, amplitude factor. For the NPSE computations performed in this work, disturbances were injected at $x_i = 152.2$ mm, which, from LST analysis, corresponds to a location closely following the neutral point (i.e. the starting point of amplification) of the main frequency $f = 450$ kHz. The latter being located at $x \approx 146.5$ mm. Regarding the amplitude factor, the dimensionalization of the shape functions is based on the wall pressure fluctuations obtained with the 2D DNS at the same location. Note that the above strategy is consistent only if there is a good agreement between the normalized LST and 2D DNS profiles in the wall region.

Fig. 11 compares the wall-normal distribution of the dimensional pressure, temperature, and velocities perturbations amplitudes from NPSE and 2D DNS at $x_i = 152.2$ mm. The deviation between the NPSE and 2D DNS profiles is due to the fact that the NPSE is completely agnostic of the perturbations that are impinging the BL. In opposite to the 2D DNS which captures the perturbations in the whole flow-field. Discrepancies in the normalization between the normal profiles from LST, NPSE and 2D DNS will tend to decrease as the pressure at the wall increases due to the amplification of the second mode instability.

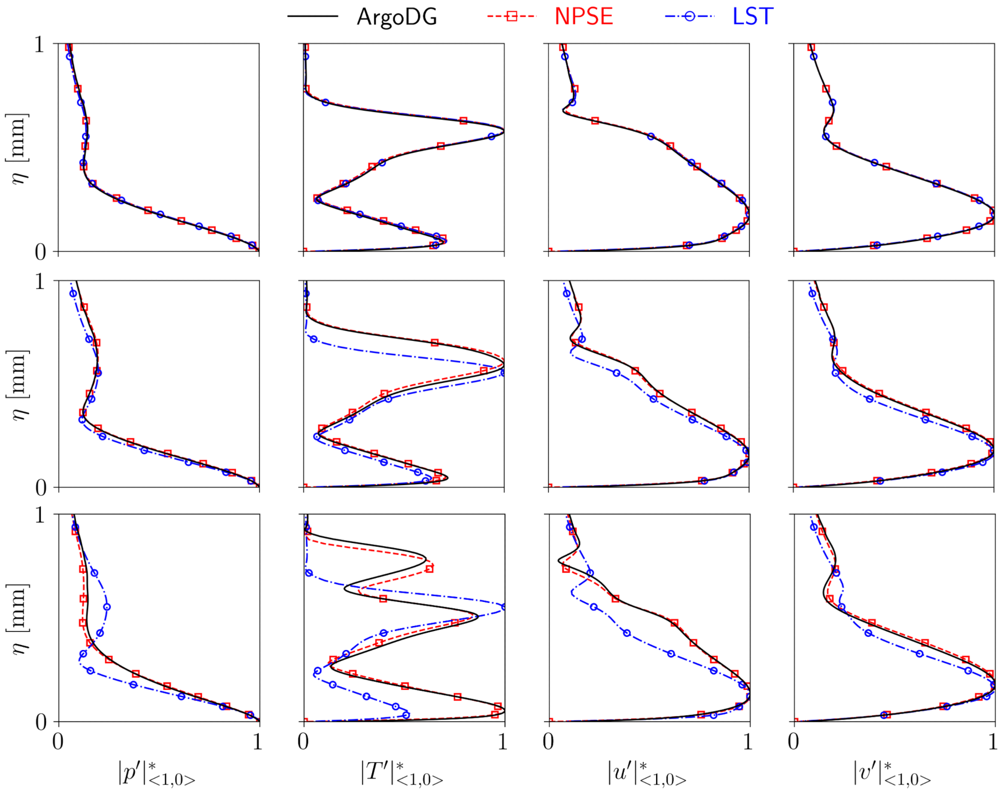

Fig. 10 Comparison between LST, NPSE and 2D DNS of the perturbations shape functions related to the main frequency $\mathbf{f_{\langle 1,0\rangle}}$ in the wall normal direction at the stations x = 180 mm (1st row), x = 220 mm (2nd row) and x = 245 mm (3rd row).

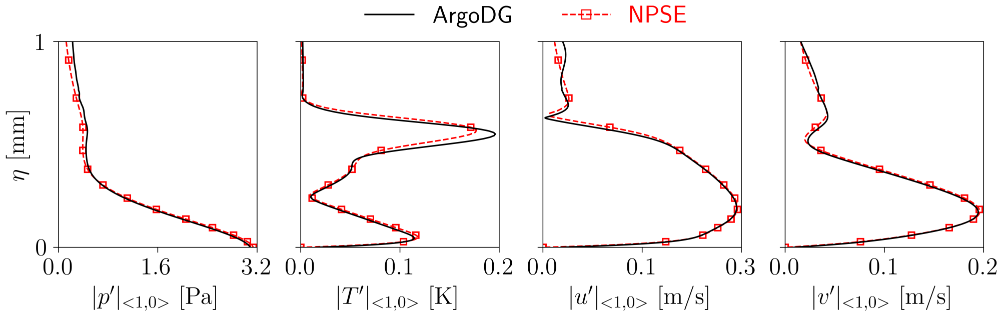

Fig. 11 Comparison between NPSE and 2D DNS of the amplitude of the pressure, temperature and velocities perturbations related to the main frequency $\mathbf{f_{\langle 1,0\rangle}}$ along the wall normal at $\mathbf{x_i}$ = 152.2 mm.

As expected, good agreements are observed at $x = 180$ mm (see Fig. 10) between all methods given the linear regime. Further downstream, the nonlinearities become more dominant, as shown in Fig. 12, therefore leading to discrepancies in the shape functions of the main frequency between the 2D DNS and the LST at $x = 220$ mm. However, a good agreement is still obtained between the 2D DNS and the predictions from the NPSE. For qualitative comparisons purposes between these two methods, the dimensional wall pressure amplitude for $f_{\langle 1,0\rangle}$ and all its harmonics is proposed in Fig. 12, where the amplitudes for $f_{\langle 1,0\rangle}$ and its first harmonic in the normal direction at $x = 220$ mm is shown in Fig. 13. Finally, similar perturbation shape functions from the NPSE and the 2D DNS are shown in Fig. 10 at $x = 245$ mm, where a third peak appears in the temperature profiles for both methods. This feature results from the broadening of the rope-like structures in that region, as illustrated in Fig. 8. Nevertheless, differences are retrieved in the location of the early stages of the nonlinear saturation regime, leading to a strong mismatch in the amplitude of the pressure fluctuations at the wall between the NPSE and the 2D DNS. The reason for this mismatch could be twofold. The first one could come from the fact that the 2D DNS is not statistically converged, leading to a biased comparison in that region. The other reason could be related to the highly nonlinear state of the flow-field in the saturation region which could make NPSE predictions less reliable.

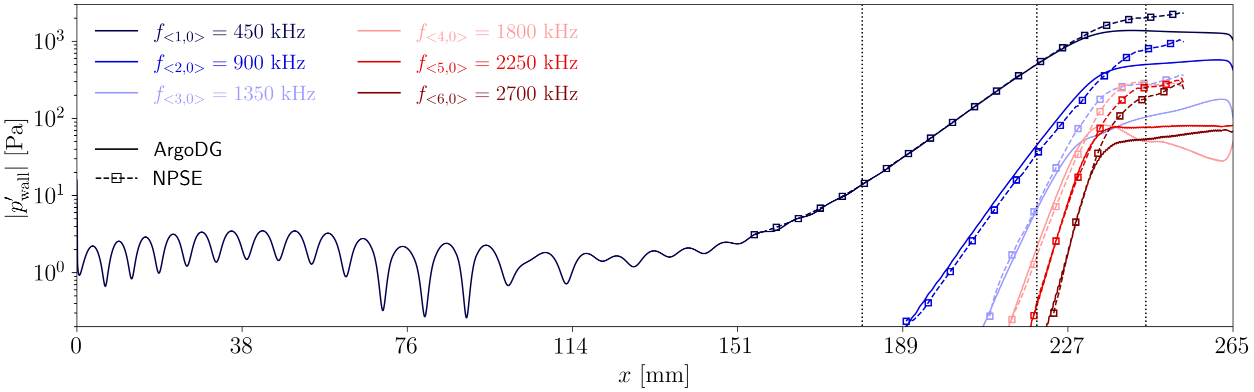

Fig. 12 Spectral distribution of the amplitude of the wall pressure perturbations from the 2D DNS and comparison with the predictions from NPSE for the first five harmonics. The stations used for the normal profiles comparisons in Fig. 10 are represented by the dotted lines.

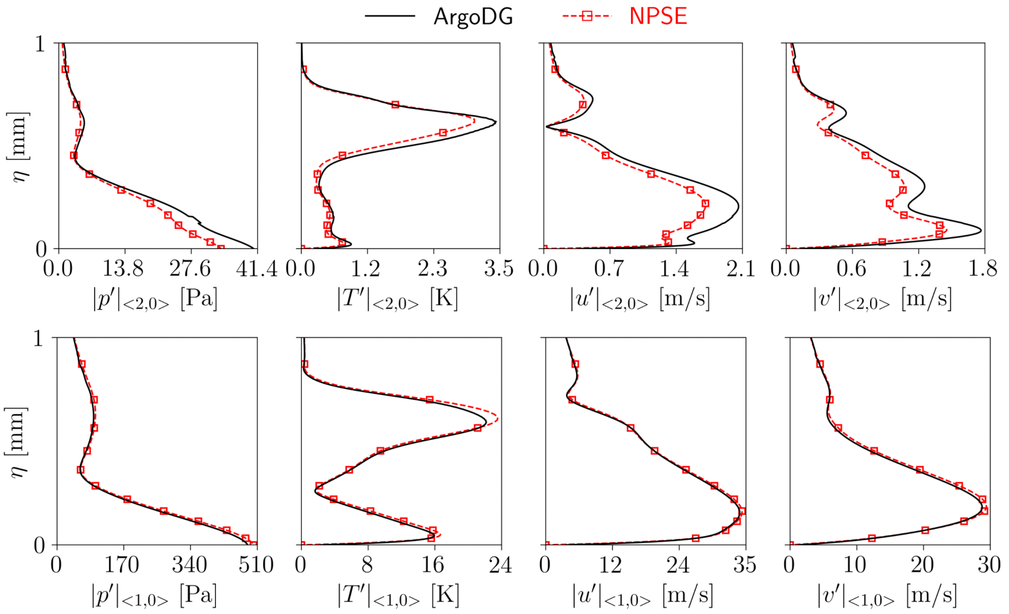

Fig. 13 Comparison between NPSE and 2D DNS of the amplitude of the pressure, temperature and velocities perturbations related to the main frequency $f_{\langle 1,0\rangle} = 450$ kHz and its first harmonic $f_{\langle 2,0\rangle} = 900$ kHz along the wall normal at $x = 220$ mm.

VI. Conclusions and Perspectives

This work studied the impact of wind-tunnel-like freestream acoustic on the amplification of the second-mode instability over the canonical blunt cone geometry. The test conditions were the ones of the H3 hypersonic facility from the von Karman Institute. First, LST has been used to retrieve the most amplified frequency related to the second mode. This frequency has then been prescribed in the time-dependent boundary conditions for the 2D DNS simulation in order to model the BL receptivity to freestream acoustic disturbances. Regarding the 2D DNS, order adaptation and scale-resolving capabilities of the DG solver allowed to capture both the strong shock and the perturbations amplification in the boundary layer. Results of the DNS have then been compared to the ones from the LST. Good agreements were observed between the two methods until a point where nonlinearities start to emerge. Therefore, additional comparisons involving NPSE have been conducted. Good matches between the profiles of the 2D DNS and the NPSE have also been obtained qualitatively, but mostly quantitatively, until the nonlinear saturation region near the end of the cone. These results motivate the dual use of NPSE and high-fidelity simulations in the modeling and the understanding of hypersonic BL. For example, high-fidelity simulations could be initialized further downstream on the body based on NPSE predictions, thus skipping the early stages of the modal growth, and eventually reducing the cost of the high-fidelity simulations. Future work will focus on the restart of the simulation with the following adjustments. The capture of the shock would be performed at high-order where the physic-based artificial viscosity presented in Section IV.A.2 would be applied to stabilize the shock. The objective here is two-fold. The first objective is to reduce the amount of numerical dissipation caused by the limiting approach. The second objective is to reduce the numerical pollution that is generated in the post-shock region due to the jump between zeroth-order and high-order elements. Finally, a finer tuning of the small parameter ε and the spectral content of the noise injection model would be applied based on observations in the VKI H3 ground testing facility [29].

Acknowledgments

The authors gratefully acknowledge the fruitful discussions they had during the NASA Ames MSV (Modeling Summer Visit 2025) program in which this work has been initiated.

A. Ghyoot thanks a lot also Ludovic Taguema, from Cenaero, for his advice and suggestions regarding the mesh generation and the data visualizations. This research is part of the Space4ReLaunch project, which is supported by the SPW Economie Emploi Recherche of the Walloon Region, under grant agreement no. 2210181. The present research benefited from computational resources made available on Lucia, the Tier-1 supercomputer of the Walloon Region, infrastructure funded by the Walloon Region under the grant agreement n°1910247.

V. Romano gratefully acknowledges the financial support of the *Fonds de la Recherche Scientifique* (F.R.S.-FNRS) of Belgium for the FRIA grant, with reference FC 58087.

G. Perrucci gratefully acknowledges the financial support of the *Université libre de Bruxelles* (ULB).

References

[1] Ma, Y., and Zhong, X., "Receptivity of a supersonic boundary layer over a flat plate. Part 3. Effects of different types of free-stream disturbances," *Journal of Fluid Mechanics*, Vol. 532, 2005, pp. 63 – 109. https://doi.org/10.1017/S0022112005003836.

[2] Choudhari, M., Chou, A., Muñoz, F., Radespiel, R., Schilden, T., Schröder, W., Marineau, E., Casper, K., Chaudhry, R., Candler, G., Gray, K., and Schneider, S., "Characterization of Freestream Disturbances in Conventional Hypersonic Wind Tunnels," *Journal of Spacecraft and Rockets*, Vol. 56, 2018, pp. 1–12. https://doi.org/10.2514/1.A34290.

[3] Lei, J., and Zhong, X., "Linear Stability Analysis of Nose Bluntness Effects on Hypersonic Boundary Layer Transition," *Journal of Spacecraft and Rockets*, Vol. 49, No. 1, 2012, pp. 24–37. https://doi.org/10.2514/1.59120.

[4] Hillewaert, K., "Development of the discontinuous Galerkin method for high-resolution, large scale CFD and acoustics in industrial geometries," Ph.D. thesis, Université catholique de Louvain, 2013. Promotor: Jean-François Remacle.

[5] Schrooyen, P., Toulorge, T., Pinna, F., Turchi, A., and Magin, T., "Towards high-order discretization method for hypersonic flow," *Proceedings of HiSST: 2nd International Conference on High-Speed Vehicle Science & Technology*, 2022.

[6] Pinna, F., "VESTA toolkit: a software to compute transition and stability of boundary layers," *43rd AIAA Fluid Dynamics Conference*, 2013, p. 2616. https://doi.org/10.2514/6.2013-2616.

[7] Grossir, G., Masutti, D., and Chazot, O., "Flow characterization and boundary layer transition studies in VKI hypersonic facilities," *53rd AIAA Aerospace Sciences Meeting*, 2015, p. 0578. https://doi.org/10.2514/6.2015-0578.

[8] Qu, F., Sun, D., Liu, Q., and Bai, J., “A Review of Riemann Solvers for Hypersonic Flows,” *Archives of Computational Methods in Engineering*, Vol. 29, 2021. https://doi.org/10.1007/s11831-021-09655-x.

[9] Romano, V., del Val, A., Magin, T., and Chazot, O., “Multiphysics Investigation of Hypersonic Boundary Layer Stability by Global Sensitivity Analysis,” *AIAA SCITECH 2026 Forum*, 2026, p. 0946. https://doi.org/10.2514/6.2026-0946.

[10] Ma, Y., and Zhong, X., “Receptivity of a supersonic boundary layer over a flat plate. Part 2. Receptivity to free-stream sound,” *Journal of Fluid Mechanics*, Vol. 488, 2003, p. 79–121. https://doi.org/10.1017/S0022112003004798.

[11] Hoskin, D. S., Heyningen, R. L. V., Nguyen, N. C., Vila-Pérez, J., Harris, W. L., and Peraire, J., “Discontinuous Galerkin Methods for Hypersonic Flows,” , 2023. URL https://arxiv.org/abs/2312.17619.

[12] Chan, J., “On discretely entropy conservative and entropy stable discontinuous Galerkin methods,” *Journal of Computational Physics*, Vol. 362, 2017. https://doi.org/10.1016/j.jcp.2018.02.033.

[13] Persson, P.-O., and Peraire, J., “Sub-Cell Shock Capturing for Discontinuous Galerkin Methods,” *44th AIAA Aerospace Sciences Meeting and Exhibit*, American Institute of Aeronautics and Astronautics, Reno, Nevada, 2006. https://doi.org/10.2514/6.2006-112, URL https://doi.org/10.2514/6.2006-112.

[14] VonNeumann, J., and Richtmyer, R. D., “A Method for the Numerical Calculation of Hydrodynamic Shocks,” *Journal of Applied Physics*, Vol. 21, No. 3, 1950, pp. 232–237. https://doi.org/10.1063/1.1699639, URL https://doi.org/10.1063/1.1699639.

[15] Chen, T., and Shu, C.-W., “Entropy stable high order discontinuous Galerkin methods with suitable quadrature rules for hyperbolic conservation laws,” *Journal of Computational Physics*, Vol. 345, 2017, pp. 427–461. https://doi.org/https://doi.org/10.1016/j.jcp.2017.05.025, URL https://www.sciencedirect.com/science/article/pii/S002199911730400X.

[16] Rueda-Ramírez, A. M., Pazner, W., and Gassner, G. J., “Subcell limiting strategies for discontinuous Galerkin spectral element methods,” *Computers amp; Fluids*, Vol. 247, 2022, p. 105627. https://doi.org/10.1016/j.compfluid.2022.105627, URL http://dx.doi.org/10.1016/j.compfluid.2022.105627.

[17] Hesthaven, J., “A Study of Several Artificial Viscosity Models within the Discontinuous Galerkin Framework,” *Communications in Computational Physics*, Vol. 27, 2020, pp. 1309–1343. https://doi.org/10.4208/cicp.OA-2019-0118.

[18] Fernandez, P., Nguyen, C., and Peraire, J., *A physics-based shock capturing method for unsteady laminar and turbulent flows*, AIAA Aerospace Sciences Meeting, doi:10.2514/6.2018-0062. https://doi.org/10.2514/6.2018-0062, URL https://arc.aiaa.org/doi/abs/10.2514/6.2018-0062.

[19] Wei, L., Zhou, L., and Xia, Y., “The jump filter in the discontinuous Galerkin method for hyperbolic conservation laws,” *Journal of Computational Physics*, Vol. 520, 2025, p. 113498. https://doi.org/https://doi.org/10.1016/j.jcp.2024.113498, URL https://www.sciencedirect.com/science/article/pii/S0021999124007460.

[20] Hartmann, R., “Adaptive discontinuous Galerkin methods with shock-capturing for the compressible Navier–Stokes equations,” *International Journal for Numerical Methods in Fluids*, Vol. 51, No. 9-10, 2006, pp. 1131–1156. https://doi.org/https://doi.org/10.1002/fld.1134, URL https://onlinelibrary.wiley.com/doi/abs/10.1002/fld.1134.

[21] Mack, L. M., *Boundary-layer stability theory*, Jet Propulsion Laboratory, 1969.

[22] Van Ingen, J., “The eN method for transition prediction. Historical review of work at TU Delft,” *38th Fluid Dynamics Conference and Exhibit*, 2008, p. 3830. https://doi.org/https://doi.org/10.2514/6.2008-3830.

[23] Chang, C.-L., Malik, M. R., Erlebacher, G., and Hussaini, M. Y., “Linear and nonlinear PSE for compressible boundary layers,” Tech. rep., 1993.

[24] Candler, G. V., Johnson, H. B., Nompelis, I., Gidzak, V. M., Subbareddy, P. K., and Barnhardt, M., “Development of the US3D code for advanced compressible and reacting flow simulations,” *53rd AIAA Aerospace Sciences Meeting*, 2015, p. 1893. https://doi.org/https://doi.org/10.2514/6.2015-1893.

[25] Capriati, M., Massari, D., and Schrooyen, P., “Development of HEROES: Hybrid Mesh Adapter for Hypersonic,” *3rd International Conference on Flight Vehicles, Aerothermodynamics and Re-entry (FAR)*, 2025.

[26] Larsson, J., and Zhong, X. (eds.), *Turbulence and Transition in Supersonic and Hypersonic Flows*, 1st ed., Academic Press, 2025. EBook ISBN: 9780443187841.

[27] Hader, C., and Fasel, H., “Nonlinear stages of transition and breakdown to turbulence: Direct numerical simulations,” *Computation and Analysis of Turbulent Flows – Turbulence and Transition in Supersonic and Hypersonic Flows*, edited by J. Larsson and X. Zhong, Academic Press, 2026, pp. 283–383.

[28] Zanus, L., and Pinna, F., “Stability Analysis of Hypersonic Flows in Local Thermodynamic Equilibrium Conditions by Means of Nonlinear PSE,” *AIAA Aviation*, 2018, p. 3696. https://doi.org/https://doi.org/10.2514/6.2018-3696.

[29] Saenz, L., Kovács, D., and Grossir, G., “Implementation of Focused Laser Differential Interferometry for Measurements in Supersonic and Hypersonic Facilities at VKI,” *AIAA SCITECH 2026 Forum*, 2026, p. 0008. https://doi.org/10.2514/6.2026-0008.